Influence of Precursor Concentration on the Sol-Gel Synthesis and Characterization of Copper Oxide Nanoparticles

Rafid Mahdi Rahman and Jasim Mohammed Alzanganawee
Department of Physics, University of Diyala, 32001 Diyala, Iraq
sciphyms232401@uodiyala.edu.iq, Alzanganawee@uodiyala.edu.iq

Keywords: CuO Nanoparticles, Sol-Gel Synthesis, Precursor Concentration, XRD, FTIR, Zeta Potential.

Abstract: Copper oxide (CuO) nanoparticles were synthesized through a sol-gel process using copper nitrate trihydrate as the metal source and citric acid as the chelating and gel-forming agent. Two precursor concentrations, 0.1 M and 0.2 M, were employed to examine their influence on structural and surface characteristics. The gels were dried at 70 °C and calcined at 450 °C to obtain fine black CuO powders. X-ray diffraction confirmed the formation of pure monoclinic CuO with average crystallite sizes of approximately 33.4 nm and 22.6 nm for the 0.1 M and 0.2 M samples, respectively. Scanning electron microscopy showed agglomerated but uniform nanostructures, and energy-dispersive spectroscopy verified elemental purity. Uv-visible spectra exhibited absorption edges near 210 nm and 191 nm, corresponding to optical band gaps that decreased slightly with concentration. FTIR spectra displayed characteristic Cu-O stretching bands between 520 and 600 cm^{-1}, confirming successful oxide formation. Zeta potential values of +10.16 mV (0.1 M) and −7.31 mV (0.2 M) indicated that increasing precursor concentration alters surface charge and reduces colloidal stability. These results demonstrate that precursor concentration is a key parameter in tuning the physicochemical behavior of CuO nanoparticles for functional applications.

1 INTRODUCTION

Nanomaterials-typically defined as having at least one dimension in the 1-100 nm range-exhibit properties that differ markedly from their bulk counterparts due to their high surface-to-volume ratios and size-dependent electronic structures. By controlling composition, size, shape, and surface chemistry, researchers have tailored nanomaterials to achieve distinctive optical, electrical, magnetic, catalytic, and mechanical behaviors suitable for diverse technologies [1]. Copper-based systems are of particular interest: both metallic copper and copper oxide nanoparticles combine earth abundance and cost-effectiveness with highly tunable physicochemical properties and relatively low toxicity, and they can be readily produced via multiple scalable methods [2]. Among transition-metal oxides, cupric oxide (CuO) stands out as an important p-type semiconductor with a narrow direct band gap (≈ 1.2 eV for bulk material, which can be further tuned in the nanoscale regime[3] Reported CuO morphologies include spheres, flowers, rods, ribbons, and platelets; these shapes influence charge transport, light absorption, and surface reactivity [4]. A broad set of synthesis routes-hydrothermal, co-precipitation, sol-gel, and green/biogenic methods-has been used to access these structures and tune particle size and defect density [5] CuO and ZnO nanostructures have been widely investigated for antimicrobial, catalytic, environmental, packaging, and biomedical uses, benefiting from their stability and functionality in aqueous and physiological environments [6]. In many of these applications, performance correlates strongly with nanoscale attributes such as crystallite size, agglomeration state, surface functional groups, and colloidal stability. Consequently, understanding how synthesis parameters influence these attributes is essential for rational design. [7]. One key yet practical parameter is precursor concentration during sol-gel processing. Varying the metal-salt concentration can modify hydrolysis-condensation kinetics and nucleation density, thereby affecting crystallite size, strain, and the extent of particle aggregation after calcination. These structural changes, in turn, influence spectroscopic signatures (e.g., FTIR and UV-Vis) and dispersion stability (e.g., zeta potential), all of which are relevant to device performance and formulation stability[8]. In this work, we synthesize CuO

nanoparticles via a citric-acid-assisted sol-gel route at two precursor concentrations (0.1 M and 0.2 M) and evaluate how this change impacts structure and surface properties. We employ X-ray diffraction (XRD) to confirm phase purity and estimate crystallite size (Scherrer and Williamson-Hall analyses), scanning electron microscopy (SEM) with energy-dispersive X-ray spectroscopy (EDS) to assess morphology and composition, FTIR to verify Cu-O bonding and residual organics, UV-Vis spectroscopy to probe optical response, and zeta potential measurements to quantify dispersion stability. By holding processing conditions constant apart from concentration, we provide a clear link between precursor concentration and key physicochemical descriptors that underpin CuO performance in catalytic, optical, sensing, and antibacterial contexts[9].

2 MATERIALS AND METHODS

Copper (II) nitrate trihydrate ($Cu(NO_3)_2•3H_2O$), citric acid ($C_6H_8O_7$), dilute aqueous ammonia (for pH adjustment), polyvinyl alcohol (PVA), and deionized water were used as received without further purification. For the 0.1 M synthesis route, 9.664 g of $Cu(NO_3)_2•3H_2O$ was dissolved in 200 mL of deionized water under continuous stirring at room temperature until a clear solution of free cupric ions was obtained (1). Separately, 7.6848 g of citric acid was dissolved in 200 mL of deionized water and added dropwise to the copper solution.

The pH of the mixture was carefully adjusted to ≈4 by the dropwise addition of dilute ammonia. Under these mildly acidic conditions, the ammonia acts as a weak base that deprotonates the citric acid (2)

The resulting citrate anions act as strong chelating agents, binding with the Cu^{2+} ions to form a highly stable and soluble copper-citrate complex (3) rather than inducing bulk precipitation. The sol was subsequently heated to ~65 °C under continuous stirring. A few drops of PVA were introduced as a structure-directing network, and the mixture was maintained at 65 °C for roughly 12 hours until a cohesive metal-organic gel was formed.

The resulting gel was dried at 80 °C for 6-8 hours and then calcined in air at 450 °C for 3 hours. During this thermal treatment, the stable copper-citrate complex undergoes direct thermolysis and oxidative decomposition (Eq4). The organic matrix and nitrate ligands are entirely burned off as volatile gases, facilitating the crystallization of the pure monoclinic CuO phase. The calcined product was gently ground to obtain a fine CuO powder. The 0.2 M sample was prepared following an identical protocol using doubled precursor weights (Fig. 1).

Reaction equations pathway:

$$Cu(NO_3)_2•3H_2O\ (aq) \rightarrow Cu^{2+}\ (aq) + 2NO_3^-\ (aq) + 3H_2O \quad (1)$$

$$C_6H_8O_7\ (aq) + 3NH_4OH\ (aq) \rightarrow C_6H_5O_7^{3-}\ (aq) + 3NH_4^+\ (aq) + 3H_2O \quad (2)$$

$$Cu^{2+}\ (aq) + C_6H_5O_7^{3-}\ (aq) \rightarrow [Cu(C_6H_5O_7)]^-\ (aq) \quad (3)$$

$$2[Cu(C_6H_5O_7)]^-\ (s) + 2NO_3^-\ (s) + 9O_2\ (g) \rightarrow 2CuO\ (s) + 12CO_2\ (g) + 5H_2O\ (g) + 2NO_2\ (g) \quad (4)$$

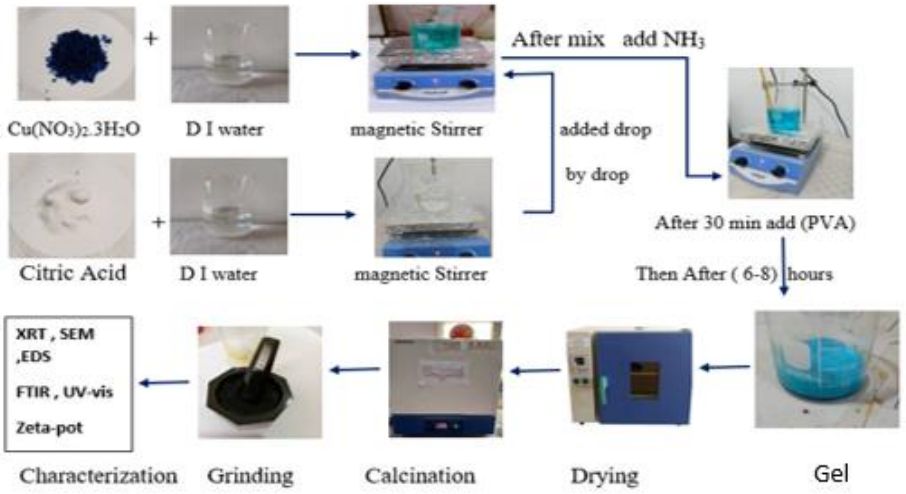

Figure 1: Steps to prepare of CuO NPs.

3 RESULTS AND DISCUSSION

3.1 XRD Analysis

XRD patterns of the calcined powders confirm single-phase monoclinic CuO (tenorite) for both precursor concentrations, consistent with standard data for CuO and prior reports. The most intense reflections appear at 2θ ≈ 35.6° and 38.7°, corresponding to the (-111) and (111) planes, respectively, with an additional high-intensity peak near 48.9° assigned to (-202) [10]. For the 0.1 M sample, the principal peaks occur at 35.58° (d ≈ 2.540 Å, (-111)), 38.74° (d ≈ 2.323 Å, (111)), and 48.87° (d ≈ 1.863 Å, (-202)), in good agreement with card CuO [00-048-1548], [11].

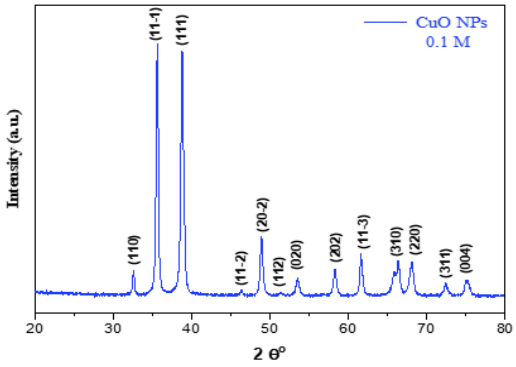

Figure 2: XRD pattern for CuO NPs (0.1M).

Figure 2 shows the X-ray diffraction plot of copper oxide nanoparticles with a concentration of 0.1 M. For the 0.2 M sample, the corresponding features are at 34.92° (d ≈ 2.569 Å,(-111)), 38.12° (d ≈ 2.364 Å, (111)), and 48.27° (d ≈ 1.885 Å, (-202)), again matching monoclinic CuO [96-410-5683] [12].

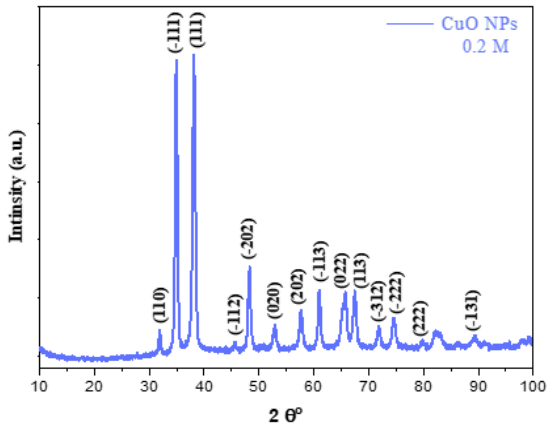

Figure 3: XRD pattern CuO NPs (0.2M).

Figure 3 shows the X-ray diffraction plot of copper oxide nanoparticles with a concentration of 0.2 M. Average crystallite sizes estimated from peak broadening give ~33.4 nm (0.1 M) and ~22.56 nm (0.2 M) by the Scherrer approach.

Solvent polarity is believed to influence the molecular mechanism, which in turn affects the properties of nanoparticles[13]. The size of copper oxide nanoparticles (Table 1) was shown to decrease with increasing molar concentrations of ($Cu(NO_3)_2•3H_2O$), while Williamson-Hall analysis yields comparable values with micro strain on the order of 10^{-2} (≈0.01 for 0.1 M and ≈0.02 for 0.2 M), indicating that the slight reduction in apparent size at higher concentration is accompanied by a small increase in lattice strain. The absence of extra reflections attributable to Cu, CuO, or other parasitic phases further supports phaspurity under the applied calcination conditions [14].Table 1 shows XRD peak parameters and crystallite size of sol-gel CuO (0.1 M and 0.2 M).

3.2 SEM Morphology of CuO NPs

SEM images of the calcined CuO powders (450 °C, 3hours) reveal nanoparticulate aggregates with concentration-dependent packing (Fig. 4a). At 0.1 M, the micrographs (500 nm field of view; (120,000×) show loosely clustered particles with predominantly spherical to sub-spherical outlines. In contrast, at 0.2 M sample (Fig.4 b) exhibits tighter, more compact agglomerates; most grains remain sub- spherical, although a fraction appears irregular at the aggregate edges. The particle size distributions (Fig. 5a) are consistent with these trends. The 0.1 M dispersion centers around an average diameter of ≈ 78.96 nm, whereas the 0.2 M material shifts (Fig. 5b) to a larger mean of ≈ 91.13 nm, indicating modest coarsening and denser packing at higher precursor concentration. Overall, the morphological evolution with concentration-looser clusters at 0.1 M versus tighter aggregates at 0.2 M-aligns with the observed shift in the size histogram and supports a concentration-driven increase in nucleation density followed by more extensive growth/coalescence during calcination under identical thermal conditions.

The apparent discrepancy between the crystallite size determined from XRD analysis and the particle size observed via SEM can be attributed to the fundamental difference in what each technique measures. XRD calculations (Scherrer and Williamson-Hall methods) determine the size of coherently scattering domains (individual crystallites), whereas SEM images the physical

morphology of the particles. The significantly larger sizes observed in SEM (~79 nm for 0.1 M and ~91 nm for 0.2 M) compared to the XRD crystallite sizes (~33.4 nm and ~22.56 nm, respectively) clearly indicate that the physical particles observed are actually polycrystalline aggregates composed of several smaller crystallites. This agglomeration is thermodynamically driven by the high surface energy of the nanoparticles and their inherently low colloidal stability. Furthermore, the Williamson-Hall (W-H) analysis confirms the presence of lattice strain within the samples. This strain likely originates from the high density of grain boundaries and structural defects formed at the interfaces where these smaller crystallites cluster together to form the larger microscopic agglomerates [14].

Table 1: XRD peak parameters and crystallite size of sol-gel CuO (0.1 M and 0.2 M).

Sample	2θ (°)	d (Å)	(hkl)	FWHM (°)	D (Scherrer, nm)	D (W-H, nm)	Micro Strain (ε)
0.1 M	35.58	2.5399	(-111)	0.3013	33.4	29.5 (W-H)	0.01
	38.74	2.3231	(111)	0.1957			
	48.87	1.8630	(-202)	0.3319			
0.2 M	34.92	2.5694	(-111)	0.2341	22.56	28.4 (W-H)	0.02
	38.12	2.3639	(111)	0.5062			
	48.27	1.8845	(-202)	0.6311			

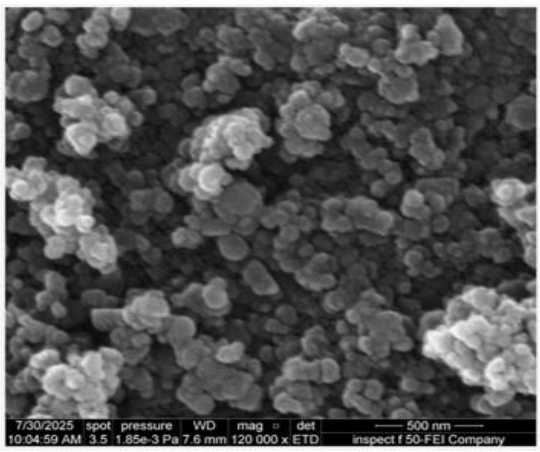

Fig (4-a)

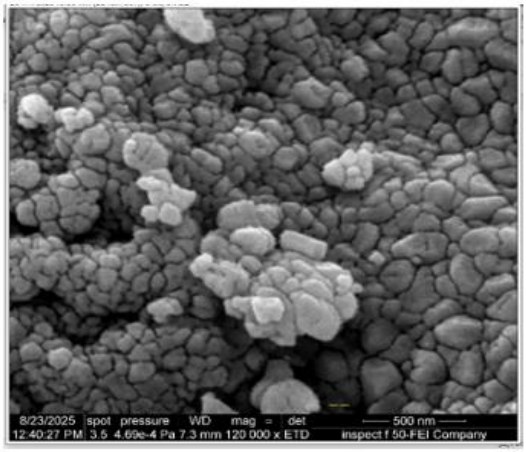

Fig (4-b)

Figure 4: SEM of CuO nanoparticles (450 °C/3 hours): a) 0.1 M-loosely clustered, mostly sub-spherical, b) 0.2 M-compact agglomerates with sub-spherical to irregular grains.

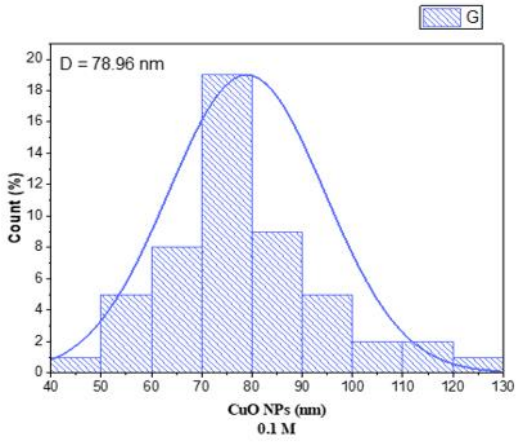

(a)

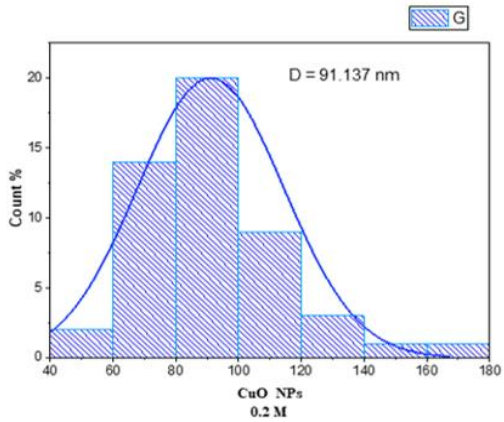

(b)

Figure 5: Particle size distributions of CuO nanoparticles: ((SEM-based image analysis), a) 0.1 M-average 78.96 nm, b) 0.2 M-average 91.13 nm.

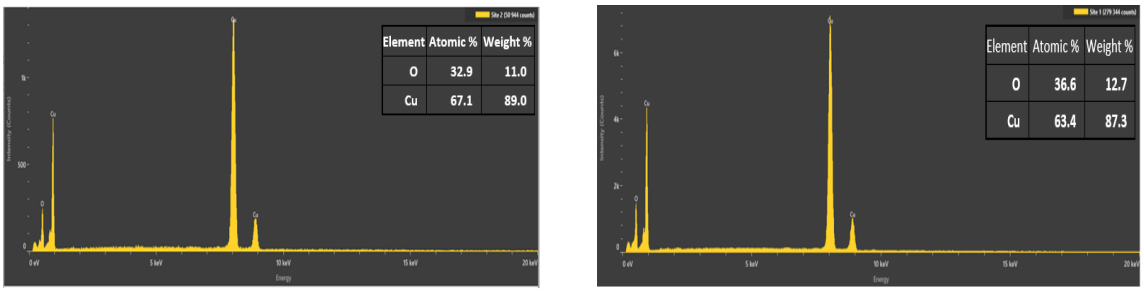

(a) (b)

Figure 6: EDS spectra of CuO nanoparticles at (a) 0.1 M and (b) 0.2 M showing Cu (0.92, ~8 keV) and O (~0.5 keV) peaks; no extraneous elements detected.

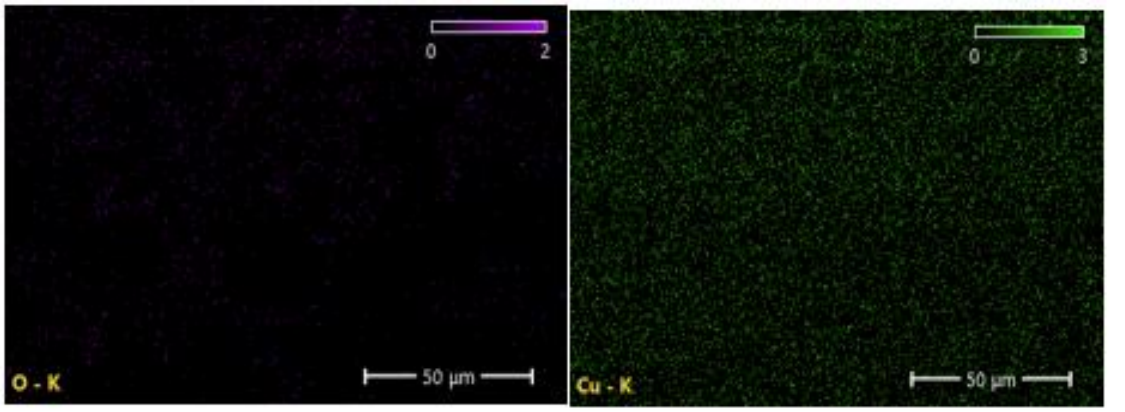

(a)

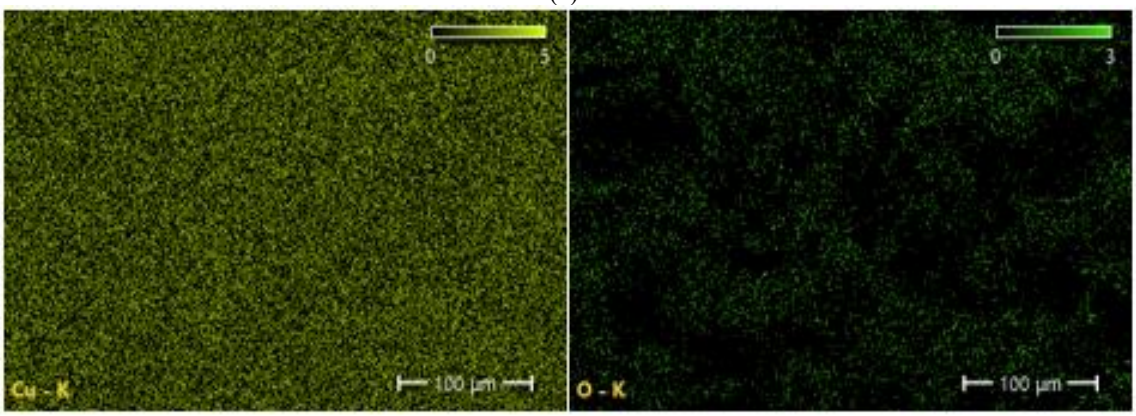

(b)

Figure 7: Elemental maps for: a) 0.1 M, b)0.2 M samples showing uniform, co-located Cu and O distribution.

3.3 Energy-Dispersive Spectroscopy (EDS)

EDS spectra for both concentrations show only copper and oxygen signals, with the Cu Lα peak near 0.92 keV, the Cu Kα/Kβ lines at higher energy (around 8 keV), and an O Kα peak at ~0.5 keV. No additional elemental peaks were detected above the background, indicating an absence of extraneous contaminants under the measurement conditions. The accompanying quantitative table (Fig. 6) lists the elemental weight and atomic percentages; after standard ZAF correction and normalization to 100%, the Cu:O ratios fall close to the expected stoichiometry for CuO within typical EDS uncertainty.

Elemental maps (Fig. 7) display a uniform and co-located distribution of Cu and O across the imaged regions for both 0.1 M and 0.2 M samples, rather than composition. We note the usual limitations of EDS-reduced sensitivity to light elements and surface roughness effects-but the combined spectra and maps

support phase purity and chemical homogeneity of the calcined powders. Microscopy (SEM) observations. Heavier precursor loads typically promote denser particle agglomeration and larger crystallite sizes This, in turn, restricts the effective optical path length and suppresses the light scattering that normally occurs in well-dispersed nano systems [15], consistent with the formation of a single copper-oxide phase. Minor variations in local intensity are attributed to topography and aggregate thickness.

3.4 Uv-Visible Results

Optical analysis of the dispersed CuO nanoparticles revealed a distinct dependency on precursor concentration, as illustrated in Figure 8. For the 0.1 M preparation, the absorbance was notably higher, featuring a prominent absorption edge in the deep-ultraviolet (UV) zone around 210 nm (A ≈ 0.236). Increasing the molarity to 0.2 M led to a diminished optical response and a slight blue shift of the edge to approximately 191 nm (A ≈ 0.07). This reduction in UV-Vis absorbance at higher molarities correlates directly with the scanning electron.

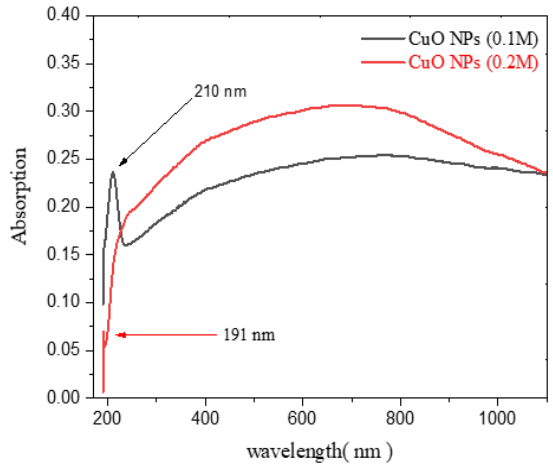

Figure 8: Uv-Vis spectra of CuO nanoparticles prepared by sol-gel: a) 0.1 M-edge near 210 nm (A ≈ 0.236), b) 0.2 M-edge near 191 nm (A ≈ 0.07).

It is well-established that cupric oxide behaves as a p-type semiconductor characterized by a relatively narrow fundamental energy gap. Consequently, the deep-UV spectral features located at 210 nm and 191 nm-equivalent to high photon energies of roughly 5.9 eV and 6.5 eV-cannot be assigned to the intrinsic band-to-band transitions of pure CuO. Instead, these high-energy absorption bands are most likely generated by ligand-to-metal charge transfers, structural defects, or residual organic impurities left over from the synthesis process [16].

To determine the actual optical band gap of the synthesized samples, we relied on the standard Tauc procedure targeting the linear segment within the visible to near-infrared spectrum. Assuming a direct allowed electronic transition, we applied the relation $(\alpha h\nu)^2$ against incident photon energy ($h\nu$). Extrapolating the linear slope to the energy axis yielded band gap values situated between 1.2 eV and 1.5 eV. This specific energy window firmly verifies the formation of the CuO phase, aligning with established literature for direct transition gaps in nanoscale cupric oxide [17].

For an accurate comparative assessment, we maintained a uniform baseline correction and an identical fitting window across both sample concentrations. This approach not only standardizes the band gap extraction but also allows us to reliably measure the Urbach energy, which represents the tailing of localized states into the gap. Figure 9: Tauc plots for the determination of the optical bandgap energy (Eg) of CuO NPs prepared at varying precursor concentrations (a- 0.1 M and b- 0.2 M) Crucially, the variations in this Urbach tailing are in strong agreement with the micro strain and lattice defect densities we calculated using the Williamson-Hall (W-H) method from X-ray diffraction (XRD) data[18] Ultimately, the noticeable attenuation and shifting of the UV absorption profiles when transitioning from 0.1 M to 0.2 M closely mirror the morphological changes and crystallite growth, pointing toward a moderate variation in surface defect states between the two synthesized batches.

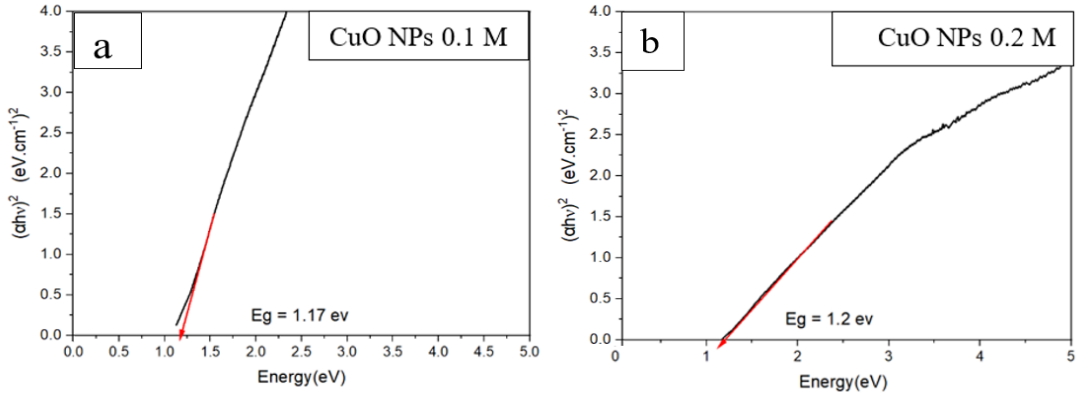

Figure 9: Tauc plots for the determination of the optical bandgap energy (Eg) of CuO NPs prepared at varying precursor concentrations a) 0.1 M, b) 0.2 M).

3.5 FT-IR Results

Fourier transform infrared spectroscopy (FT-IR) was employed to elucidate the surface functional groups, chemical coordination, and structural bonding of the synthesized nanoparticles. Figure 10 presents the FT-IR spectra of the samples prepared at 0.1 M and 0.2 M precursor concentrations. The bands observed in the high-frequency region, specifically at 3666.68 cm^{-1} (0.1 M) and the broader features at 3479.58 and 3051.39 cm^{-1} (0.2 M), are attributed to the stretching vibrations of distinct

O-H groups. These arise from physically adsorbed water molecules and varying degrees of hydrogen-bonded surface hydroxyls, which readily bind to the active surface sites of the high-surface-area nanoparticles. Chemically, the peaks observed at 1645.28, 1504.48, and 1454.33 cm^{-1} should not be viewed merely as physical residues; rather, they correspond predominantly to the asymmetric and symmetric stretching vibrations of carboxylate (COO^{-}) groups. This indicates the chemical coordination and chelation of citrate ligands (or their intermediate derivatives) onto the CuO surface during the sol–gel synthesis. Similarly, the absorption bands at 1070.49 cm^{-1} (0.1 M) and 1145.72 cm^{-1} (0.2 M) are assigned to C-O stretching vibrations associated with these coordinated organic species. In the fundamental fingerprint region, the bands at 848.68 and 740.67 cm^{-1} are characteristic of Cu–O–Cu bridging vibrations. Most importantly, the strong, well-defined bands at 535.35 cm^{-1} (0.1 M) and 528.50 cm^{-1} (0.2 M) represent the fundamental infrared-active phonon modes (typically Au or Bu modes) of the Cu–O stretching vibrations in the monoclinic crystal lattice. These specific metal-oxygen vibrational modes provide conclusive structural evidence for the successful formation of single-phase CuO [19].

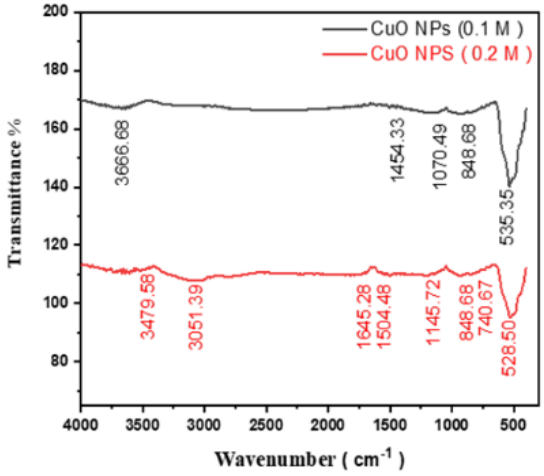

Figure 10: Fourier transform infrared spectroscopy (FTIR) analysis.

3.6 Zeta Potential

Zeta potential measurements were performed to evaluate the surface charge and colloidal stability of the synthesized CuO nanoparticles. Figure 11 illustrates the zeta potential distributions for the samples prepared at 0.1 M and 0.2 M precursor concentrations. The results show that the CuO sample synthesized at 0.1 M exhibits a zeta potential of +10.16 mV, whereas the sample prepared at 0.2 M displays a value of -7.31 mV. It is important to emphasize that both absolute values fall well below the typical threshold required for strong electrostatic stabilization (typically ($|\zeta| > 30$ mV). Consequently, the nanoparticles in both systems exhibit inherently

low colloidal stability and a high thermodynamic tendency to agglomerate, which is consistent with the particulate clustering commonly observed in pristine metal oxide synthesis.

However, the most critical observation is the distinct charge reversal from positive to negative as the precursor concentration increases. At the lower concentration (0.1 M), the slight positive charge suggests that the nanoparticle surface is predominantly influenced by uncompensated Cu^{2+} ions. Conversely, at the higher concentration (0.2 M), the increased concentration of reactants likely promotes a higher surface adsorption of hydroxyl ($-OH^{-}$) or other oxygen-containing anionic species. This preferential adsorption outcompetes the positive surface sites, shifting the net surface charge to a negative value.

In conclusion, rather than a transition from a stable to an unstable dispersion, the increase in precursor concentration drives a fundamental modification in the surface chemistry (charge reversal) while maintaining an overall weak electrostatic repulsion, further explaining the agglomerated morphology of the samples [20], [21].

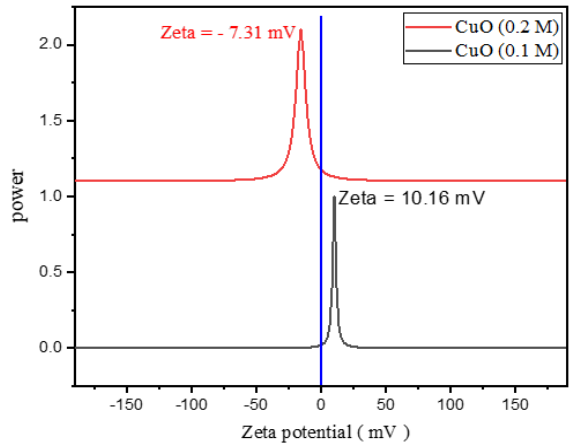

Figure 11: Zeta potential of CuO concentration (0.1M) and concentration (0.2M).

4 CONCLUSIONS

Copper oxide nanoparticles were produced using the sol-gel method with the aid of citric acid at two concentrations of the starting material, all other conditions being constant. X-ray diffraction (XRD) confirmed the presence of monoclinic, monophasic copper oxide in both samples, confirming the success of the preparation process. The expected crystal structure was formed, and all recorded peaks belonged to copper oxide, with no additional peaks, indicating the purity of the prepared oxide. Calculations using the Scherrer formula showed a slight decrease in the average crystal size from about 33.4 nm (0.1 mol) to about 22.56 nm (0.2 mol), which corresponds to a slight increase in lattice stress at the higher concentration. Despite this change, the crystal sizes remained within the nanoscale. Scanning electron microscopy (SEM) images showed a shift from more flexible agglomerates at 0.1 mol to denser agglomerates at 0.2 mol, with corresponding average particle sizes of about 79 nm and 91 nm, respectively. UV-Vis spectra showed deep UV-Vis edges near 210 nm (0.1 mol) and 191 nm (0.2 mol). The presence of the 210 nm edge is attributed to a π-π^* transition, and zeta potential measurements indicated a change in surface charge and dispersion stability with concentration: +10.16 mV at 0.1 mol and -7.31 mV at 0.2 mol. Taken together, these results demonstrate that simply increasing the starting material concentration is an effective way to control the crystal size, agglomeration state, optical response, and surface charge of sol-gel-prepared copper oxide nanoparticles, which is relevant for applications in catalysis, sensing, and antibacterial formulations.

REFERENCES

[1] B. Mekuye and B. Abera, “Nanomaterials: An overview of synthesis, classification, characterization, and applications,” Nano Select, vol. 4, no. 8, 2023, [Online]. Available: https://doi.org/10.1002/nano.202300038.

[2] M. I. Din and R. Rehan, “Synthesis, characterization, and applications of copper nanoparticles,” 2017, [Online]. Available: https://doi.org/10.1080/00032719.2016.1172081.

[3] S. Naz, A. Gul, M. Zia, and R. Javed, “Synthesis, biomedical applications, and toxicity of CuO nanoparticles,” 2023, [Online]. Available: https://doi.org/10.1007/s00253-023-12364-z.

[4] A. A. Thamer, M. Noor Hussein, S. H. Imran, and R. H. Hassani, “Sol-gel process optimization for CuO nanoparticle synthesis achieving high purity and homogeneity,” Journal of Physics: Conference Series, vol. 2974, no. 1, 2025, [Online]. Available: https://doi.org/10.1088/1742-6596/2974/1/012019.

[5] H. T. Gebrie, et al., “Biosynthesis and characterization of copper oxide nanoparticles from Plumbago zeylanica leaf extract for antibacterial and antioxidant activities,” Scientific Reports, vol. 15, no. 1, pp. 1-16, 2025, [Online]. Available: https://doi.org/10.1038/s41598-025-10700-z.

[6] N. Paper and P. Submission, “Synthesis of zinc oxide nanoparticles via sol-gel route and their characterization,” Journal of Nanoscience and Nanotechnology, vol. 5, pp. 2010-2014, 2016, [Online]. Available: https://doi.org/10.5923/j.nn.20150501.01.

[7] H. He, Q. Yang, J. Wang, and Z. Ye, "Layer-structured ZnO nanowire arrays with dominant surface- and acceptor-related emissions," Materials Letters, vol. 65, no. 9, 2011, [Online]. Available: https://doi.org/10.1016/j.matlet.2011.01.080.

[8] C. Satari, R. S. Sidqi, R. F. Putra, S. R. Putri, and A. B. D. Nandiyanto, "Literature review: synthesis of CuO (copper oxide) nanoparticles for thermal energy storage," International Journal of Energetica, vol. 6, no. 2, p. 21, 2021, [Online]. Available: https://doi.org/10.47238/ijeca.v6i2.176.

[9] S. S. Millavithanachchi, et al., "Green synthesis, optimization, and characterization of CuO nanoparticles using Tithonia diversifolia leaf extract," Nanomaterials, vol. 15, no. 15, pp. 1-16, 2025, [Online]. Available: https://doi.org/10.3390/nano15151203.

[10] A. A. Khalefa, J. M. Marei, H. A. Radwan, and J. M. Rzaij, "In2O3-CuO nano-flakes prepared by spray pyrolysis for gas sensing application," Digest Journal of Nanomaterials and Biostructures, vol. 16, no. 1, pp. 197-204, 2021, [Online]. Available: https://doi.org/10.15251/djnb.2021.161.197.

[11] O. Diachenko, et al., "Structural and optical properties of CuO thin films synthesized using spray pyrolysis method," Coatings, vol. 11, no. 11, 2021, [Online]. Available: https://doi.org/10.3390/coatings11111392.

[12] J. Jońca, et al., "Organometallic synthesis of CuO nanoparticles: Application in low-temperature CO detection," ChemPhysChem, vol. 18, no. 19, pp. 2658-2665, 2017, [Online]. Available: https://doi.org/10.1002/cphc.201700693.

[13] O. Of, "Ournal of," vol. 31, no. 4, pp. 886-890, 2019.

[14] H. Jensen, et al., "Determination of size distributions in nanosized powders by TEM, XRD, and SAXS," Journal of Experimental Nanoscience, vol. 1, no. 3, pp. 355-373, 2006, [Online]. Available: https://doi.org/10.1080/17458080600752482.

[15] S. Sachdeva and I. Choudhary, "Photoluminescent characteristics of solution-processed nanoscale copper oxide," Materials Physics and Mechanics, vol. 52, no. 6, pp. 27-37, 2024, [Online]. Available: https://doi.org/10.18149/MPM.5262024_4.

[16] B. Balamurugan and B. R. Mehta, "Optical and structural properties of nanocrystalline copper oxide thin films prepared by activated reactive evaporation," Thin Solid Films, vol. 396, no. 1-2, pp. 90-96, 2001, [Online]. Available: https://doi.org/10.1016/S0040-6090(01)01216-0.

[17] E. Arulkumar, S. Thanikaikarasan, S. Rajkumar, and W. Wondimu, "Influence of solution pH dependency on structure, optical with photoelectrochemical characteristics of SILAR deposited copper oxide thin films," Heliyon, vol. 10, no. 13, 2024, [Online]. Available: https://doi.org/10.1016/j.heliyon.2024.e33579.

[18] C. Gherasim, M. Asandulesa, N. Fifere, F. Doroftei, D. Tîmpu, and A. Airinei, "Structural, optical and dielectric properties of some nanocomposites derived from copper oxide nanoparticles embedded in poly(vinylpyrrolidone) matrix," Nanomaterials, vol. 14, no. 9, 2024, [Online]. Available: https://doi.org/10.3390/nano14090759.

[19] A. S. Ethiraj and D. J. Kang, "Synthesis and characterization of CuO nanowires by a simple wet chemical method," Nanoscale Research Letters, vol. 7, 2012, [Online]. Available: https://doi.org/10.1186/1556-276X-7-70.

[20] J. M. Berg, A. Romoser, N. Banerjee, R. Zebda, and C. M. Sayes, "The relationship between pH and zeta potential of ~30 nm metal oxide nanoparticle suspensions relevant to in vitro toxicological evaluations," Nanotoxicology, vol. 3, no. 4, pp. 276-283, 2009, [Online]. Available: https://doi.org/10.3109/17435390903276941.

[21] S. Bhattacharjee, "DLS and zeta potential – What they are and what they are not?," Journal of Controlled Release, vol. 235, pp. 337-351, 2016, [Online]. Available: https://doi.org/10.1016/j.jconrel.2016.06.017.